Strong Laser Emission Modulation by Coherent Perfect Absorption inside complex-coupled Distributed Feedback Laser Diodes

Yaoyao Liang, Jean-rené Coudevylle, Henri Benisty, Abderrahim Ramdane, Anatole Lupu

Strong Laser Emission Modulation by Coherent Perfect Absorption inside complex-coupled Distributed Feedback Laser Diodes

Yaoyao Liang, Jean-René Coudevylle, Henri Benisty, Abderrahim Ramdane, and Anatole Lupu[*]

Y. Liang, J-R. Coudevylle, A. Ramdane, A. Lupu
Centre de Nanosciences et de Nanotechnologies, CNRS, Université Paris-Saclay, C2N – 10 Boulevard Thomas Gobert – 91120 Palaiseau cedex, France
E-mail: anatole.lupu@c2n.upsaclay.fr

H. Benisty
Laboratoire Charles Fabry, Université Paris-Saclay, Institut d'Optique IOGS, 2 Avenue A Fresnel, 91120 Palaiseau, France

Keywords: coherent perfect absorption, DFB lasers, laser-modulator, complex-coupled Bragg grating, non-Hermitian photonics, Parity-Time symmetry

Abstract:
The proof-of-concept of the exploitation of Coherent Perfect Absorption (CPA) in electrically-injected distributed-feedback laser sources is reported. Capitalizing on the essence of CPA as "light extinction by light", an integrated laser-modulator scheme emerges. The key ingredient compared to conventional single-frequency laser diodes is a careful periodic in-phase modulation of both real and imaginary parts of the complex grating index profile that enables both single frequency operation and 40 dB line purity at the Bragg frequency. We show that this combination is most apt for the operation of CPA as a modulation mechanism that respects the laser spectral purity. The specific proof-of-concept is based on an ultra-short external cavity formed by a metallic micro-mirror, whose role is to generate the second beam of more conventional CPA interferometric approaches. The implemented complex-coupled grating is compatible with existing industrial technologies and promising for real-life laser source applications. Furthermore, the concept can be directly transferred to other material platforms and other wavelengths ranging from terahertz to ultraviolet.

1. Introduction

Non-Hermitian systems in optics have gained a lot of momentum recently.[1-7] Parity-Time symmetry is a typical example of systems where specific architectures of loss and gain bring a wealth of new physical effects and applications.[8-14] A specific case of nontrivial interplay of losses with field structure is coherent perfect absorption (CPA) also known as Borrmann effect.[15-27] In CPA, the nodes of the electric field profile are made to coincide with spatially localized loss structures, e.g. thin layers, wires, etc.[28-37] Typically a standing wave pattern formed by two phase-adjusted contrapropagative waves provides the capability to control the phenomenon.

Reported realizations are numerous but nearly none has addressed real-life devices such as edge-emitting lasers.[38-42] We propose in this paper a novel form of CPA implementation that enables novel device architectures: the use of CPA in the very emitting medium of a laser itself, operating optimally in synergy with a grating inscribed in the laser, as is common in distributed feedback (DFB) laser diodes, a workhorse of modern photonics.

We illustrate this idea in **Figure** 1. It consists of a DFB laser diode (typically of mm-sized cavity length) with an external cavity of optical thickness of a few wavelengths at most. Qualitatively, the external mirror imposes the phase of the reflected wave, which in turn,

through the various interferences, shifts the pattern of the standing wave. In the schematic example of Figure 1a, d1 and d2 differ by λ/4, thus the pattern of antinodes is shifted by the same amount, swapping antinodes and nodes. Assuming that a non-Hermitian pattern (of gain and/or of loss) has the same periodicity as the antinodes (vertical stripes), one of the two position favors gain and the other favors loss. The concept of "lasing and antilasing" based on a set of two probe beams highlighted the same physics.[39] If the antinodes of the standing waves produced by the two beams coincide the largest gain zones, this results in amplified emission, and the opposite otherwise.

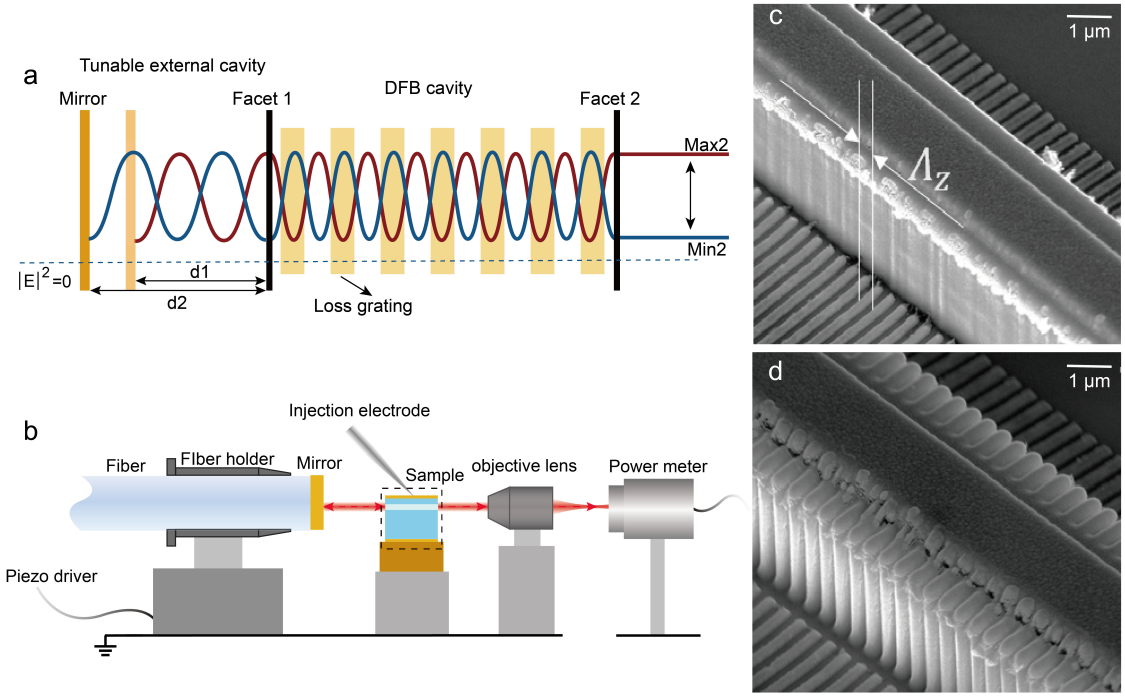

Figure 1. a) Sketch of a DFB laser with lossy Bragg and external cavity formed by a high reflectivity metallic mirror. b) Schematic of the experimental setup with 200 nm thick gold micro-mirror deposited on a cleaved facet of an optical fiber and mounted on a translation stage with piezo-driver controller. c) Micrograph of gold wires Bragg grating and III-V semiconductor waveguide. d) Micrograph of complex-coupled Bragg grating waveguide.

Until now, these demonstrations were based on a pair of external beams, obtained by usual "bulky" photonic methods. Here, we propose to apply this concept with the laser source itself, using a strongly reflected lightwave travelling in a short external auxiliary cavity as the "second beam". This is akin to the operation of the so-called "Salisbury screen",[43-45] but using the internal loss-modulated Bragg-grating DFB laser as amplifier or absorbing medium as a function of the phase associated with the external cavity length. In both cases, the absorbing/gain medium (a sheet or a grating) is seen very differently according to the reflected phase.

The main application that we propose based on our proof-of-principle is an integrated laser modulator. Indeed, the modulation of laser diode emission is a delicate photonic engineering topic. Direct electrical modulation is often plagued by frequency chirp due to the large change in carrier density. External modulation by fast modulators is the majority scheme in optical communications, typically based on electro-absorption (electro-absorption modulator, EAM) induced by the quantum-confined Stark Effect (QCSE) that modulates a QW oscillator strength.[46-48] The implementation of QCSE or more generally EAM inside laser diodes themselves was barred from consideration mainly due to the residual losses of EAM, impairing efficient laser operation.

In our proof-of-principle demonstration, the modulation relies on the mechanical motion of a close external mirror, but any short "phase section" could perform a similar job. Since the 1990s, established "phase shifter section" have been implemented in various complex tunable monolithic DFB and DBR (Distributed Bragg Reflector) laser diodes with typical size in the 300-500 µm range. [49-53] Tunability is achieved by modifying the injection current and hence the concentration of free carriers in the phase control section transparent at the laser frequency. Additionally, modulation technologies for integrated photonics have been boosted by the general effervescence around silicon photonics. [54,55] To date, silicon-based modulators (for telecom) can reach dimensions as short as ~100 µm, which is already comparatively small for a > 1mm-long active-section device. Furthermore, there are some avenues based on exotic materials (III-V, oxides) that could bring higher efficiency and telecom-compatible rates (> 10 GHz).[56] Given this context, with changes that could be more than incremental, it seems timely to invoke the possibility of a sub-100 µm efficient phase shifter as one of the ingredients in a device that would incorporate our CPA proposal.

Ultimately, compared to directly-modulated lasers or to above-mentioned EAM based on carrier-induced electro-absorption, an external-cavity-based modulation based on the antilasing concept would not suffer from similar limitations. Thus, we believe it has the ability to compete with the fastest stand-alone electro-optic modulators. As for the absorption losses incurred by non-Hermitian operation in our case, it will be seen that a careful choice of the grating causes only very modest degradation of such core metrics such as the threshold current.

Conversely, one key advantage of our scheme is that CPA takes place on the whole laser cavity length, hence a strong modulation can be achieved between the limit cases of CPA (maximum absorption) and near-transparency for the complementary standing wave pattern (Figure 1a). From a theoretical standpoint, we use conventional linear plane-wave analysis to get the lasing poles of the structure and grasp the main behavior of the different types of investigated gratings and the role of specific facets.

It is worth noting that the DFB lasers used in our work have an arbitrary faceted termination, highly reflective outer mirrors, and an additional external cavity. Thus, this study goes beyond canonical PT-symmetric systems, consolidates and further propels the idea that simultaneous lasing and anti-lasing can be achieved in gain-loss modulated systems without true PT symmetry.[23] This opens the way to the extension of the CPA laser concept to a new type of gain-loss modulated architectures distinctly different from the PT-symmetric ones. The important feature is that, in a nutshell, the CPA and lasing behavior is still based on the principle of constructive-destructive interference in a gain-loss modulated structures.

The rest of paper is organized as follows. In Section 2 we describe the setup and the type of lasers used in the experiments. The moving mirror is based on a metal-coated cleaved optical fiber (the exact procedure is depicted in the SM). We next describe the modulation achieved by this technique for the different kinds of lasers, showing the superior performance of lasers with complex-coupled (C-C) Bragg grating.

In Section 3, we provide a modal gain threshold analysis of our devices, discussing the interplay of the grating and the facets for threshold gain g_{th} and side modes suppression ratio (SMSR). The analysis is also used to explore optimal configurations for future devices. Some avenues for the actual implementation of such optimal devices are suggested. The concept also lends itself to revisit the issue of DFB laser optimization even without modulation, and to connect it to the broader area of non-Hermitian and Parity-Time-symmetric photonic devices.

2. Experimental

2.1 Laser diode structures

We have investigated two different kinds of laser to assess the role of CPA and the combined role of losses and feedback for the proposed proof-of-principle of our "CPA-inside-laser"

proposal. All lasers are based on a structure similar to that used for the earlier demonstration of the Parity-Time symmetric edge-emitting DFB laser operating around 1.55 µm wavelength.[57] It consists of a 2-quantum well (QW) active layer embedded in an InGaAsP separate confinement heterostructure (SCH), epitaxially grown in an industrial-grade factory. Details on DFB lasers technological fabrication process are presented in Section S1 (Supporting Information). Figure 1c and 1d show the image of the waveguide structure for metallic grating and for C-C grating respectively. The ridge height is 1.8 µm and its width is also 1.8 µm. The metallic gratings are made from gold stripes. It is their innermost part, close to the ridge, that essentially interacts with the waveguide modes. As for the C-C grating, they rely on an optimized etching step that defines a square first-order DFB dielectric corrugation on the side of the ridge, whose typical dimensions are a transverse width of 250 nm and a 50% duty cycle of the square corrugation. The period is adapted to the waveguide mode effective index, being here Λ=240 nm for DFB operation at $\lambda \approx 1.56$ µm. The Au stripes are aligned to the teeth of the corrugation, which means that the imaginary index modulation is in-phase with the real index modulation. Bars of several lasers were cleaved, the present results come from a single cleaved bar, hence the same laser length of 1.56 mm, and identical cleaved facets, only the periodic grating is changed among the compared laser diodes.

2.2 Experimental setup

Bars are laid onto a copper plate, and the top up, so that a 125-µm-diameter fiber can be approached with usual precision means. Here, a NA=0.6 lens collects the light output (Figure 1b) and on the opposite facet, we position the gold-coated fiber that serves as an external mirror with a piezoelectric motion controller. We are able to achieve physical contact between the mirror and the laser, in a repeatable fashion, without damaging the facet thanks to a loose enough jacket holding the fiber in the piezo holder. We can control the mirror position with ~20 nm steps. The mirror motion was best assessed through the laser output oscillatory pattern, whose observed period is obviously a half-wavelength in air.

We perform the following kinds of measurements: at a given mirror position, we perform spectral measurements (OSA analyzer with 10 pm resolution), as well as "L-I" light-current characteristics with different electrical duty cycles (5% to 100%) adapted to minimize the noise of the measurement and avoid the heating of the unsoldered device. The main interesting data, however, are the power modulation curves obtained when moving the mirror, typically over 8 µm (~10 $\lambda/2$).

We note for practitioners that the "external" feedback from such short length is very far from the regime impairing the coherence of the laser (and for which isolators are needed on actual telecom laser modules for instance), and is also still far from what the conventional literature considers as an "external cavity".[58] The huge Free Spectral Range of our very short external cavity is broader than any of the relevant spectral features. The beam divergence causes a slow decrease of the amount of light actually reflected into the laser's guided mode, but there is quite some room in this respect as sizable modulations are still seen up to a distance d~20 µm. Hence, especially when we operate in the vicinity of the facet, the mirror's main effect is to drive the laser's standing wave pattern quite effectively, since the other facet only has the $R \approx 0.28$ classical reflectivity of cleaved ridges.

2.3 Experimental results

Figure 2 shows the variation of the power emitted by the metallic Bragg grating DFB laser as a function of d, the external cavity length. Marked oscillations of the power are seen with the period exactly corresponding to $\Delta d = \lambda_0/2$ at the emission wavelength λ_0 of the DFB laser. For small injection currents I = 25 mA, the emitted intensity varies from ~300 µW to only a few µW for several cycles.

The emission spectra (Figure 2d and 2e) measured at the first minimum (labeled D1) and the first peak (labeled P1) show that the single lasing mode (as expected from metallic DFB) is modulated by 50 dB. Note also that not only the lasing mode but also amplified spontaneous emission (ASE) just around it is depressed for the D1 position, due to destructive interferences.

The light-current characteristics, Figure 2b, displays the marked variation of the threshold current with cavity length, from ~20 mA (P1) to ~30 mA (D1).

Above the highest threshold value of 30 mA, the modulation of emission intensity is less contrasted, as lasing emission is permitted even at D1 position. The oscillation patterns from 25 mA to 50 mA have a gentle and similar oscillatory behavior. The corresponding spectra (Figures 2c to 2k) remain perfectly single-mode with a high SMSR. There is a small red-shift, due to the thermal drift of the laser not soldered to the copper heat sink, this attribution being assessed by the presence of the same shift for DFB laser operation without external cavity ("no mirror").

At higher injection currents around 100 mA, the modulation pattern along the cavity scan becomes jagged (Figure 2i to 2q). The kinks and extrema of this stable pattern are labeled by a1…f1, a2…f2, etc. (see inset). The emission spectra all along this cavity-length scan are distinctly different from the previous ones. They are essentially broadened (×4 to ×7 versus the low-current ones), with an appearance of multimodal emission. Note that all kinks of the various families (a, b, …) have very similar spectra. The interplay of the external cavity with the full physics of the lasing medium itself is thus reproducible and responsible for these patterns. Thus, such behavior suggests that in spite of a good wavelength selection mechanism at low currents, this kind of grating is not suitable for an extended range of injection current and laser emission power operation.

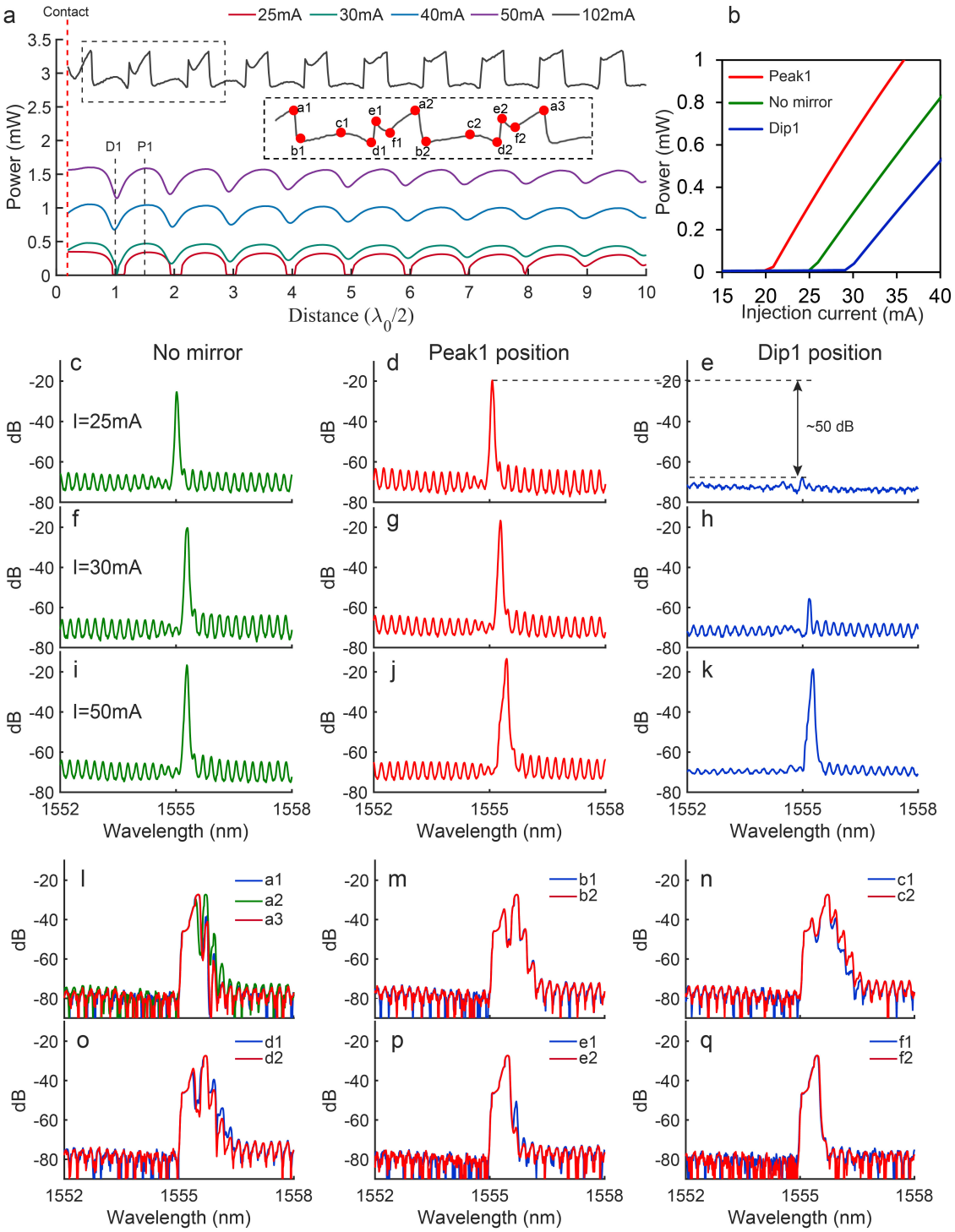

Figure 2. Metallic Bragg grating DFB laser experimental results. a) Laser emission power variation as function of external cavity length (in λ_0 units) for different injection currents. The physical contact position with laser facet indicated by red vertical dashed line. b) Light-current characteristics at external cavity mirror positions D1, P1 and also without mirror. c – q) Emission spectra as function of external cavity mirror position for different injection currents: c – e) I=25 mA; f – h) I=30 mA; i – k) I=50 mA; l – q) I=100 mA.

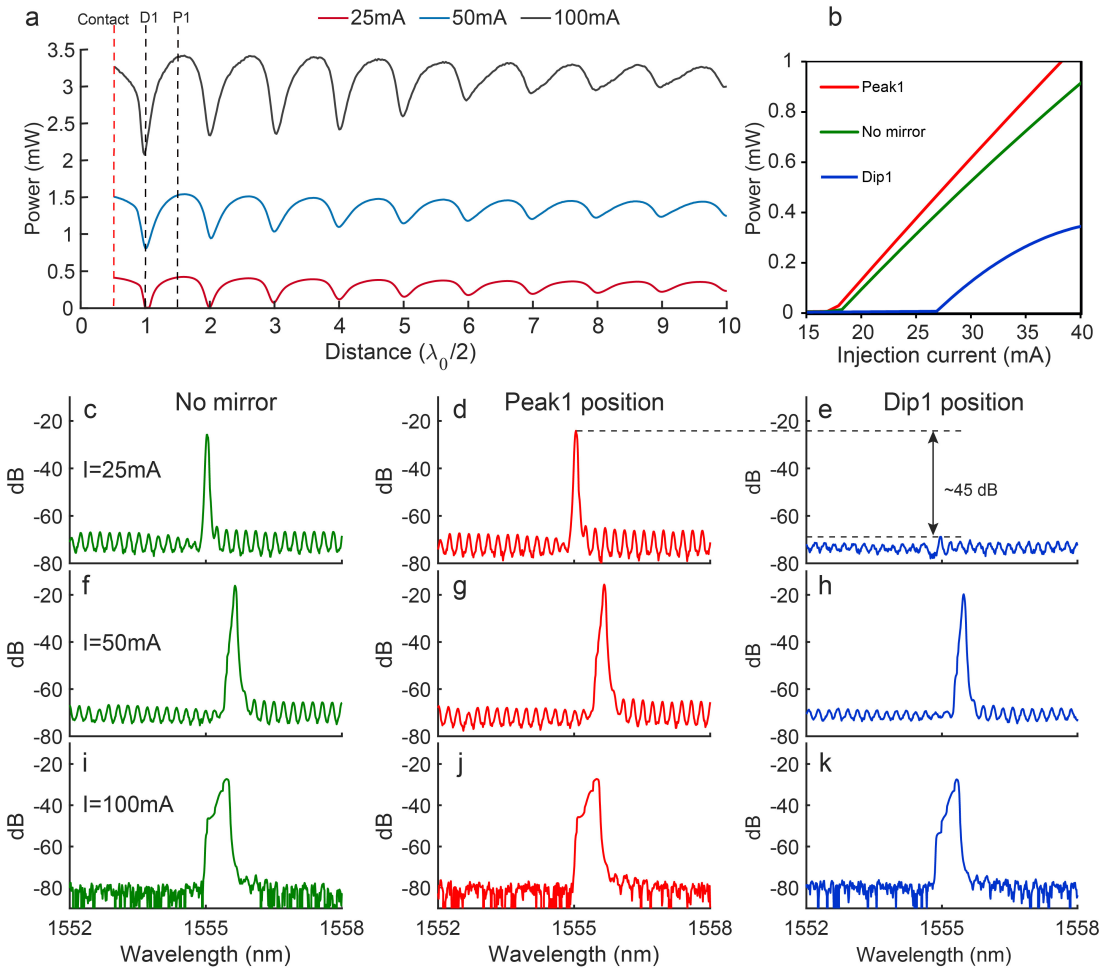

Figure 3. C-C Bragg grating DFB laser experimental results. a) Laser emission power variation as function of external cavity length (in λ_0 units) for different injection currents. The physical contact position with laser facet indicated by red vertical dashed line. b) Light-current characteristics at external cavity mirror positions D1, P1 and also without mirror. c – k) Emission spectra as function of external cavity mirror position for different injection currents: c – e) I=25 mA; f – h) I=50 mA; i – k) I=100 mA.

The origin of such behavior is discussed in Section 3 based on the modal gain threshold analysis. The same analysis suggests that C-C DFB lasers with in-phase modulation of real and imaginary index profiles should be more robust with respect to the issue of laser emission line broadening. To assess the validity of the modeling predictions, C-C DFB lasers were fabricated within the same technology cycle (Figure 1d). The experimental results are summarized in **Figure** 3. As can be seen in Figure 3a, the variation of the power emitted by the C-C DFB laser as a function of the length of the external cavity presents marked oscillations of period $\Delta d = \lambda_0/2$. Unlike the metal Bragg grating DFB laser, the oscillations pattern displays a smooth and similar oscillatory behavior even at an injection current of up to 100 mA. Furthermore, above 50 mA for a given current, the spectral shape of the laser line does not depend on the external length of the cavity. The experimental results indeed prove that CPA modulation efficiency is improved by using DFB with combined dielectric and metallic gratings (either in phase or antiphase). This is due to the decrease of the lowest gain pole with respect to the case of only metallic DFB, as discussed below. Details on the

experimental characterization techniques used for this study are presented in Section S2 (Supporting Information).

3. Modal gain threshold analysis

To get insight on the origin of the behavior seen in the experiments, the modeling results performed for a conventional plane-wave model for 1-mm-long 1st order Bragg gratings (see SM) are presented in **Figure** 4 to grasp the DFB lasers lasing poles and the related behavior.[59] The output spectral intensity at a given gain level corresponding to the onset of the lowest gain lasing mode is shown as a function of external cavity length z as a colormap in Figure 4a for the case of the metallic grating, studied first. From the spectral viewpoint, the grating just reinforces the line coinciding with the Bragg wavelength of 1.56 µm in this example. There is some influence of the external cavity value on the selected wavelength near the best lasing values (z=0.1 and z=1.1, the red part of the stripe, whose colormap is purposely saturated in these areas), but the slope is still steep. This is confirmed by Figure 4b, showing the transmission spectra for two z values, z=0.1 (maximum) and z=0.9 (minimum), corresponding to D1 and P1 in Figure 2a at low injection currents. The strong modulation of the intensity among these two cases is readily manifested by this simple model. The analysis of the poles on Figure 4c shows the z-dependence of the pole. After its minimum at z=0.1, it goes up relatively slowly on the long-wavelength side till z=0.25, where it reaches the same height as the z=0 case. This provides some indirect clues for the broadening of the laser emission at higher currents: The wavelength selection mechanism seems weaker on this "red" side of the Bragg wavelength, and it is the spectral area where broadening is observed. The secondary peaks for these 0.1<z<0.25 values are also lower on the red side. So this grating makes the wavelength selection more prone to destabilization (in the form of multimode behavior) on this red side, in the form of inhomogeneous broadening.

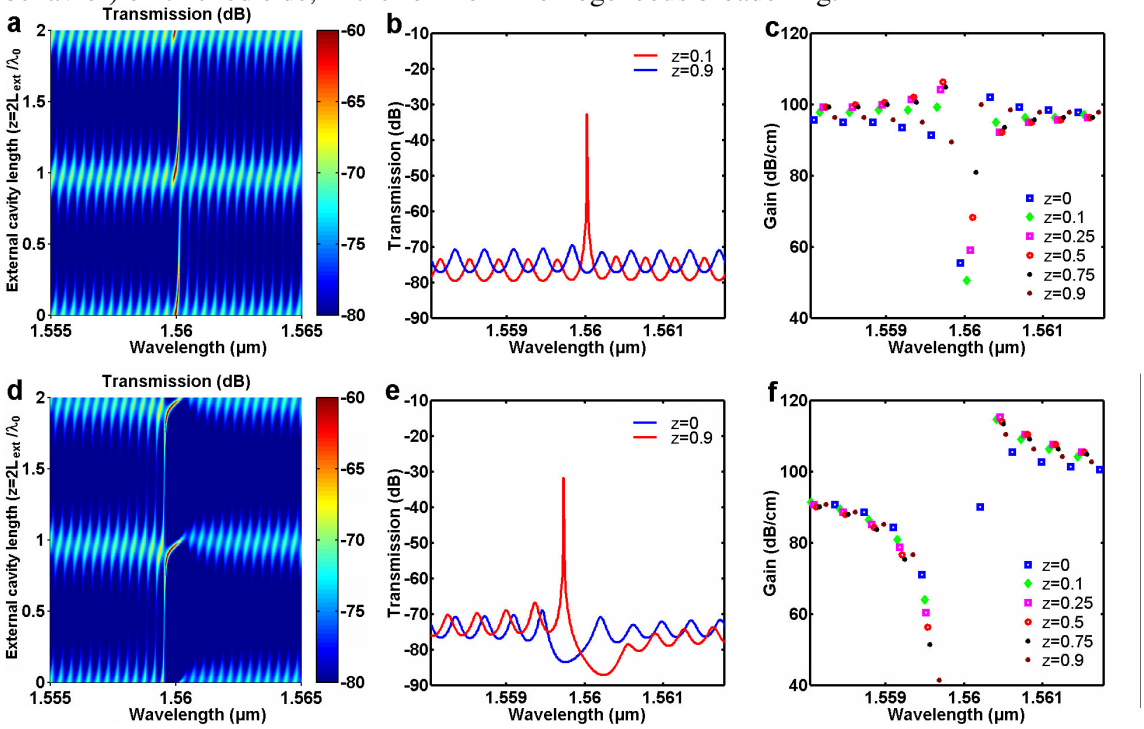

Figure 4. Modal threshold gain analysis for metallic DFB laser (a-c) and C-C DFB laser (d-f) along the same $2\lambda_0$ scan of the external cavity length ($\Delta z=2$). (a,d) Variations of the transmission intensity as a function of wavelength and z; (b,e) Transmission spectra at z corresponding to the lowest pole gain level g_{th} for the red-labelled curve, i.e., the onset of laser emission at the indicated z value, and displaying inhibited lasing for the blue-labelled

curve at the indicated z; (c,f) Map of the position of the transmission matrix poles for different external cavity length values. The lowest gain levels are g_{th} = 51dB/cm at z=0.1 for (c), metallic DFB laser, green dot; and g_{th} = 46dB/cm for (f) C-C DFB laser, brown dot.

Turning to the model for the complex-grating case, Figure 4d to 4f, we have a quite different landscape. Due to the presence of a dominant real-index modulation, the bandgap of about 1 nm width, appears as the dark blue central stripe. The lowest poles (Figure 4f) are now located at the short-wavelength-edge of the Bragg bandgap (Figure 4d and 4e), and are situated at z=0.9, z=1.9 etc.). As for the modulation dynamics, it is again strongly marked, as appears in the simple model for the two curves at z=0.5 and z=0.9 corresponding to D1 and P1 in Figure 3a.

The shape of the "crest" of Figure 4d around the pole at z=0.9 has a much lower slope than for the metallic grating. This might be one of the elements explaining the better single mode behavior of this laser structure. It is also known that the stability of lasers is different on the two sides (red and blue) of the lasing line, due to the dynamic polarizability effects of semiconductor lasers.[60] The simulations show that further improvement of performances can be achieved by considering PT-symmetric Bragg grating with AR coating (8%) of one facet.[61]

4. Summary and conclusions

We have provided a proof-of-principle demonstration of the effect of Coherent Perfect Absorption using a C-C DFB laser's own internal emission, with a short external cavity mirror instead of the two beams of the conventional CPA implementations. It can also be seen as a distributed version of the physics of the so-called "Salisbury mirror".

The investigated approach goes beyond current wisdom on this topic by considering CPA lasers substantially differing from canonical PT-symmetric systems. Its aim is to propose an affordable way to bring the CPA laser into the realm of practical applications. The obtained performances are not in any case ultimate, they can be further improved, notably by optimization of the complex-grating design.

The compactness of the considered concept opens new avenues towards the elaboration of integrated laser-modulator, where modulation is based on "light extinction by light". Electro-optic "phase sections" in integrated optics are commonly investigated nowadays to reach compact implementation schemes in diverse geometries, e.g. in silicon photonics, and the progresses along these lines could be directly transferred in our proposed design. The issue of facet phases, i.e. their position with respect to the DFB grating, would have to be addressed in each specific context.

The simplicity and robustness of our experimental method based on the use of an adjustable short length external cavity and not requiring expensive experimental equipment opens the possibility for the widespread studies of gain-loss modulated structures aiming at in-depth investigation of some theoretical concepts, in particular to track the position of the lasing poles and CPA zeros in the complex frequency plane. This should fuel a further impetus for the development of non-Hermitian optics both in theoretical and experimental domains.

In addition, the extension of the concept to the range of stimulated emission sources from THz to ultraviolet is attractive to both engineers, physicist, and material-science practitioners. Complex gratings can indeed be implemented on a variety of material platforms from III-V semiconductors to silicon photonics, and from polymers to plasmonic and associated gain-carrying nanostructures. Agile materials such as graphene, perovskite or others (quantum dots, etc.) could be envisioned for this purpose.

Acknowledgements

This work was partially funded by the French Agence Nationale pour la Recherche (project "PARTISYMO", contract number N° ANR-18-CE24-0024). Funding by the China Scholarship Council is acknowledged by Y. L (grant number 201906750021).

This work was done within the C2N micro nanotechnologies platforms and partly supported by the RENATECH network and the General Council of Essonne.

The authors warmly thank L. Couraud for his expert help in manufacturing the gold micro-mirror.

References

[1] C. M. Bender and S. Boettcher, Real spectra in non-Hermitian Hamiltonians having PT symmetry, *Phys. Rev. Lett.* **1998**, 80 5243.
[2] C. M. Bender, Making sense of non-Hermitian Hamiltonians, *Rep. Prog. Phys.* **2007**, 70(6), 947.
[3] N. Moiseyev, *Non-Hermitian quantum mechanics*, Cambridge University Press, **2011**.
[4] L. Feng, R. El-Ganainy and L. Ge, Non-Hermitian photonics based on parity–time symmetry, *Nat. Photonics.* **2017**, 11(12), 752–762.
[5] R. El-Ganainy, K. Makris, M. Khajavikhan Z. H. Musslimani, S.Rotter and D. N. Christodoulides, Non-Hermitian physics and PT symmetry, *Nature Phys*. **2018**, 14, 11–19.
[6] Y. Ashida, Z. Gong, and M. Ueda, Non-hermitian physics, *Adv. Phys.* **2020**, 69(3), 249–435.
[7] M. Liertzer, L. Ge, A. Cerjan, A. D. Stone, H. E. Türeci and S. Rotter, Pump-induced Exceptional Points in Lasers above Threshold, *Phys. Rev. Lett.* **2012**, 108(17), 173901.
[8] A. A. Zyablovsky, A. P. Vinogradov, A. A. Pukhov, A. V. Dorofeenko and A. A. Lisyansky, PT-symmetry in optics *Phys.-Usp.* **2014**, 57, 1063.
[9] C. Hang, G. Huang, and V. V. Konotop, "Tunable spectral singularities: coherent perfect absorber and laser in an atomic medium," *New. J. Phys.* **2016**, 18, 085003.
[10] H. Zhao and L. Feng, Parity–time symmetric photonics *Natl. Sci. Rev.* **2018**, 5(2), 183–199.
[11] Ş. K. Özdemir, S. Rotter, F. Nori and L. Yang, Parity–time symmetry and exceptional points in photonics *Nature Mater.* **2019**, 18(8), 783–798.
[12] A. Krasnok, D. G. Baranov, H. Li, M. A. Miri, F. Monticone, and A. Alú, Anomalies in light scattering. *Adv. Opt. Photonics* **2019**, 11(4), 892–951.
[13] A. Novitsky, D. Lyakhov, D. Michels, A. A. Pavlov, A. S. Shalin, and D. V. Novitsky, Unambiguous scattering matrix for non-Hermitian systems, *Phys. Rev. A* **2020**, 101(4), 043834.
[14] A. Krasnok, N. Nefedkin, and A. Alù, Parity-time symmetry and exceptional points [electromagnetic perspectives] *IEEE Antennas Propag. Mag.* **2021**, 63(6), 110–121.
[15] G. Borrmann, Über extinktionsdiagramme der röntgenstrahlen von quarz, *Phys. Z.* **1941**, 42, 157.
[16] G. Borrmann, Die absorption von röntgenstrahlen im fall der interferenz, *Z. Phys.* **1950**, 127, 297.
[17] G. Borrmann and W. Hartwig, *Z. Kristallogr. -Cryst. Mater.* **1965**, 121, 401.
[16] V. B. Novikov and T. V. Murzina, "Borrmann effect in photonic crystals," *Opt. Lett.* **2017**, 42, 1389–1392.
[18] S. Longhi, PT-symmetric laser absorber. *Phys. Rev. A* **2010**, 82(3), 031801.
[19] Y. D. Chong, L. Ge, H. Cao and A. D. Stone, "Coherent perfect absorbers: time-reversed lasers," *Phys. Rev. Lett.* **2010**, 105(5), 053901.
[20] Y. D. Chong, L. Ge, and A. D. Stone, PT-symmetry breaking and laser-absorber modes in optical scattering systems. *Phys. Rev. Lett.* **2011**, 106(9), 093902.

[21] N. Gutman, A. A. Sukhorukov, Y. D. Chong, and C. M. de Sterke, "Coherent perfect absorption and reflection in slow-light waveguides," *Opt. Lett.* **2013**, 38, 4970–4973
[22] R. Bruck, and O. L. Muskens, "Plasmonic nanoantennas as integrated coherent perfect absorbers on SOI waveguides for modulators and all-optical switches" *Opt. Express* **2013**, 21, 27652–27661.
[23] L. Ge, and L. Feng, "Contrasting eigenvalue and singular-value spectra for lasing and antilasing in a PT-symmetric periodic structure," *Phys. Rev. A* **2017**, 95(1), 013813.
[24] M. F. Limonov, M. V. Rybin, A. N. Poddubny, and Y. S. Kivshar, "Fano resonances in photonics," *Nat Photonics.* **2017**, 11(9), 543–554.
[25] V.A. Bushuev, B.I. Mantsyzov, Asymmetric Borrmann Effect in a Passive PT-Symmetric Photonic Crystal*, J. Exp. Theor. Phys*. **2022**, 135, 277–284 (2022).
[26] J. Bertolotti, Absorbing light using time-reversed lasers *Science* **2022**, 377,924–925.
[27] H. M. Hill, Time-reversed laser absorbs nearly all light, *Phys. Today* **2022**, 75 (11), 21–22.
[28] B. Wang, T. Koschny, and C. M. Soukoulis, "Wide-angle and polarization-independent chiral metamaterial absorber," *Phys. Rev. B* **2009**, 80, 033108.
[29] R. Alaee, M. Farhat, C. Rockstuhl, and F. Lederer, "A perfect absorber made of a graphene micro-ribbon metamaterial," *Opt. Express* **2012**, 20, 28017–28024.
[30] S. Zhong and S. He, "Ultrathin and lightweight microwave absorbers made of mu-near-zero metamaterials," *Sci. Rep.* **2013**, 3, 2083.
[31] X. Xiong, S.-C. Jiang, Y.-H. Hu, R.-W. Peng, and M. Wang, "Structured metal film as a perfect absorber," *Adv. Mater.* **2013**, 25, 3994–4000.
[32] Y. Ra'di, C. R. Simovski, and S. A. Tretyakov, "Thin perfect absorbers for electromagnetic waves: theory, design, and realizations," *Phys. Rev. Appl.* **2015**, 3, 037001.
[33] X. Fang, K. F. MacDonald, and N. I. Zheludev, "Controlling light with light using coherent metadevices: all-optical transistor, summator and invertor," *Light Sci. Appl.* **2015**, 4, e292.
[34] L. Baldacci, S. Zanotto, G. Biasiol, L. Sorba, and A. Tredicucci, "Interferometric control of absorption in thin plasmonic metamaterials: general two port theory and broadband operation," *Opt. Express* **2015**, 23, 9202–9210.
[35] M. A Kats, and F. Capasso, "Optical absorbers based on strong interference in ultra-thin films," *Laser Photonics Rev.* **2016**, 749, 735–749.
[36] D. G. Baranov, A. Krasnok, T. Shegai, A. Alù and Y. Chong, Coherent perfect absorbers: linear control of light with light, *Nature Rev. Mater.* **2017**, 2(12), 1–14.
[37] J. Zhang, X. Wei, M. Premaratne, and W. Zhu, "Experimental demonstration of an electrically tunable broadband coherent perfect absorber based on a graphene–electrolyte–graphene sandwich structure. Photonics Res. **2019**, 7(8), 868–874.
[38] W. Wan, Y. Chong, L. Ge, H. Noh, A. D. Stone and H. Cao, Time-reversed lasing and interferometric control of absorption," *Science* **2011**, 331, 889.
[39] Z. J. Wong, Y. L. Xu, J. Kim, K. O'Brien, Y. Wang, L. Feng and X. Zhang, Lasing and anti-lasing in a single cavity, *Nat. Photonics.* **2016**, 10(12), 796–801.
[40] R. Alaee, Y. Vaddi and R. W. Boyd, Dynamic coherent perfect absorption in nonlinear metasurfaces, *Opt. Lett.* **2020**, 45(23), 6414-6417.
[41] C. Wang, W. R. Sweeney, A. D. Stone and L. Yang, Coherent perfect absorption at an exceptional point, *Science* **2021**, 373(6560), 1261-1265.
[42] Y. Slobodkin, G. Weinberg, H. Hörner, K. Pichler, S. Rotter and O. Katz, Massively degenerate coherent perfect absorber for arbitrary wavefronts, *Science* **2022**, 377(6609), 995–998.
[43] W. Salisbury, "Absorbent body for electromagnetic waves," *US Patent 2599944*, **1952**.
[44] R. L. Fante, and M. T. McCormack, "Reflection properties of the Salisbury screen," *IEEE Trans. Antennas Propag.* **1988**, 36, 1443–1454.

[45] B. Chambers, Optimum design of a Salisbury screen radar absorber *Electron. Lett.* **1994**, 30 (16), 1353-1354.
[46] D. A. B. Miller, D. S. Chemla, and S. Schmitt-Rink, Electroabsorption of highly confined systems: Theory of the quantum-confined Franz–Keldysh effect in semiconductor quantum wires and dots. *Appl. Phys. Lett.* **1988**, 52(25), 2154.
[47] D. Delprat, A. Ramdane, L. Silvestre, A. Ougazzaden, F. Delorme, and. S. Slempkes, 20-Gb/s integrated DBR laser-EA modulator by selective area growth for 1.55-µm WDM applications. *IEEE Photon. Technol. Lett.* **1997**, 9(7), 898–900.
[48] N. El Dahdah, G. Aubin, J. C. Harmand, A. Ramdane, A. Shen, F. Devaux, A. Garreau and B. E. Benkelfat, Ultrafast InGaAs/InGaAlAs multiple-quantum-well electro-absorption modulator for wavelength conversion at high bit rates. *Appl. Phys. Lett.* **2004,** 84(21), 4268–4270.
[49] T. Numai, S. Murata, and I. Mito, 1.5 µm tunable wavelength filter using a phase-shift-controlled distributed feedback laser diode with a wide tuning range and a high constant gain. *Appl. Phys. Lett.* **1989**, 54(19), 1859–1860.
[50] S. Murata, and I. Mito, Frequency-tunable semiconductor lasers. *Opt. Quantum Electron.* **1990**, 22, 1–15.
[51] Numai, T. 1.5 µm phase-shift-controlled distributed feedback wavelength tunable optical filter. *IEEE J. Quantum Electron.* **1992**, 28(6), 1513–1519.
[52] V. Jayaraman, Z. M. Chuang, and L. A. Coldren, Theory, design, and performance of extended tuning range semiconductor lasers with sampled gratings. *IEEE J. Quantum Electron.* **1993**, 29(6), 1824–1834.
[53] X. He, W. Li, J. Zhang, X. Huang, J. Shan, and D. Huang, Theoretical analysis of widely tunable external cavity semiconductor laser with sampled fiber grating. *Opt. Commun.* **2006**, 267(2), 440–446.
[54] A. Rahim, A. Hermans, B. Wohlfeil, D. Petousi, B. Kuyken, D. Van Thourhout, and R. Baets, Taking silicon photonics modulators to a higher performance level: state-of-the-art and a review of new technologies. *Adv. Photonics* **2021,** 3(2), 024003–024003.
[55] L. Deniel, E. Weckenmann, D. Perez Galacho, C. Lafforgue, S. Monfray, C. Alonso-Ramos, L. Bramerie, F. Boeuf, L. Vivien and D. Marris-Morini, Silicon photonics phase and intensity modulators for flat frequency comb generation. *Photonics Res.* **2021**, 9(10), 2068–2076.
[56] M. Thomaschewski, and S. I. Bozhevolnyi, Pockels modulation in integrated nanophotonics. *Appl. Phys. Rev.* **2022**, 9(2).
[57] V. Brac de la Perrière, Q. Gaimard, H. Benisty, A. Ramdane, and A. Lupu, Electrically injected parity-time symmetric distributed feedback laser diodes (DFB) for telecom applications *Nanophonics* **2021**, 10(4), 1309–1317.
[58] R. P. Salathé, "Diode lasers coupled to external resonators," *Appl. Phys.* **1979**, 20(1), 1–18.
[59] M. Born and E.Wolf, *Principles of optics: electromagnetic theory of propagation, interference and diffraction of light*, Elsevier, **2013**.
[60] A. Bogatov, P. Eliseev, and B. Sverdlov, "Anomalous interaction of spectral modes in a semiconductor laser," *IEEE J. Quantum Electron.* **1975**, 11(7), 510–515.
[61] H. Benisty, V. Brac de la Perrière, A. Ramdane, A. Lupu, "Parity-time Symmetric gratings in 1550 nm Distributed-Feedback lasers diodes: insight on device design rules," *J. Opt. Soc. Am. B* **2021**, 38, C168–C174.

Supporting Information

Strong Laser Emission Modulation by Coherent Perfect Absorption inside complex-coupled Distributed Feedback Laser Diodes

Yaoyao Liang, Jean-René Coudevylle, Henri Benisty, Abderrahim Ramdane, and Anatole Lupu[*]

S1. Fabrication process

For the fabrication of complex-coupled (C-C) refractive index profile Bragg grating assisted lasers we considered a conventional DFB laser heterostructure, like that used for the demonstration of the Parity-Time symmetric DFB laser emitting toward 1.55 µm wavelength.[1] It consists of a 2-quantum well (QW) active layer embedded in an InGaAsP separate confinement heterostructure (SCH), grown by Gas Source Molecular Beam Epitaxy (GSMBE). The two quantum wells are surrounded by quaternary layers of different bandgaps to ensure confinement of the amplified modes, and a P-I-N junction is formed by P and N doping of the InP cladding layers.

Figure S1 shows the main technological stages of the manufacturing process of C-C DFB lasers. Given the multiple electron beam lithography (EBL) steps for the entire manufacturing process, the first is setting marks on the top of the wafer to ensure proper alignment throughout the subsequent process flow. Each EBL step is followed by metal deposition (generally Titanium (Ti)/Gold (Au)) by means of a lift-off process using Acetone/Isopropanol solutions. The *p*-contact electrode was made by a second EBL exposure.

After that, a Si_3N_4 layer with a thickness of about 300 nm is deposited on top of the III-V wafer by plasma-enhanced chemical vapor deposition (PECVD) using Unaxis D200 equipment to create a hard mask for subsequent dry etching. Transfer of the laterally corruhated Bragg grating waveguide pattern onto Si_3N_4 is achieved using a Ge/Al mask defined by a third EBL exposure, followed by deposition and lift-off of a Ge/Al layer. Then, a sulfur hexafluoride-trifluoromethane (SF_6-CHF_3) plasma in the Nextral NE 100 Capacitively Coupled Reactive Ion Etching (CCP-RIE) system is used to etch the unprotected regions of the Si_3N_4 and by this transfer the patterns on this hard mask used for Bragg grating etching.

Then, the key step of dry semiconductor etching is carried out using an inductively coupled plasma reactive ion (ICP-RIE) etching machine (SENTECH SI 500 etching system). To bring the DFB gratings as close as possible to the propagation mode, the InGaAs contact layer, the InP cladding as well as the SCH and higher layers are entirely etched. The Ge/Al mask is also removed during this step.

After that, the hard mask is removed using the same SF_6-CHF_3 based plasma in CCP-RIE. Before fabricating the metal grating, a thin insulating layer (~10 nm) of SiO_2 is deposited by the atomic layer deposition (ALD) technique for electrical insulation purposes. The metal Bragg grating pattern us defined by a fourth EBL exposure, followed by deposition of an approximately 50 nm Ti layer and conventional lift-off process.

The next step after the fabrication C-C DFB ridge waveguide structures is the surface planarization achieved by spinning and curing of about 2µm benzocyclobutene (BCB) layer. The sample is then baked at 250°C.

After that, the BCB is etched by CCP-RIE using an O_2-SF_6 plasma to open access to the *p*-contacts on the top of the ridge waveguides which are then connected to large width metal

electrodes used for current injection. The manufacturing of these metal electrodes is carried out by a fifth and final EBL exposure followed by metallization and lift-off.
The final fabrication steps are the thinning of the InP substrate, polishing and deposition ohmic contacts on the backside of the laser.

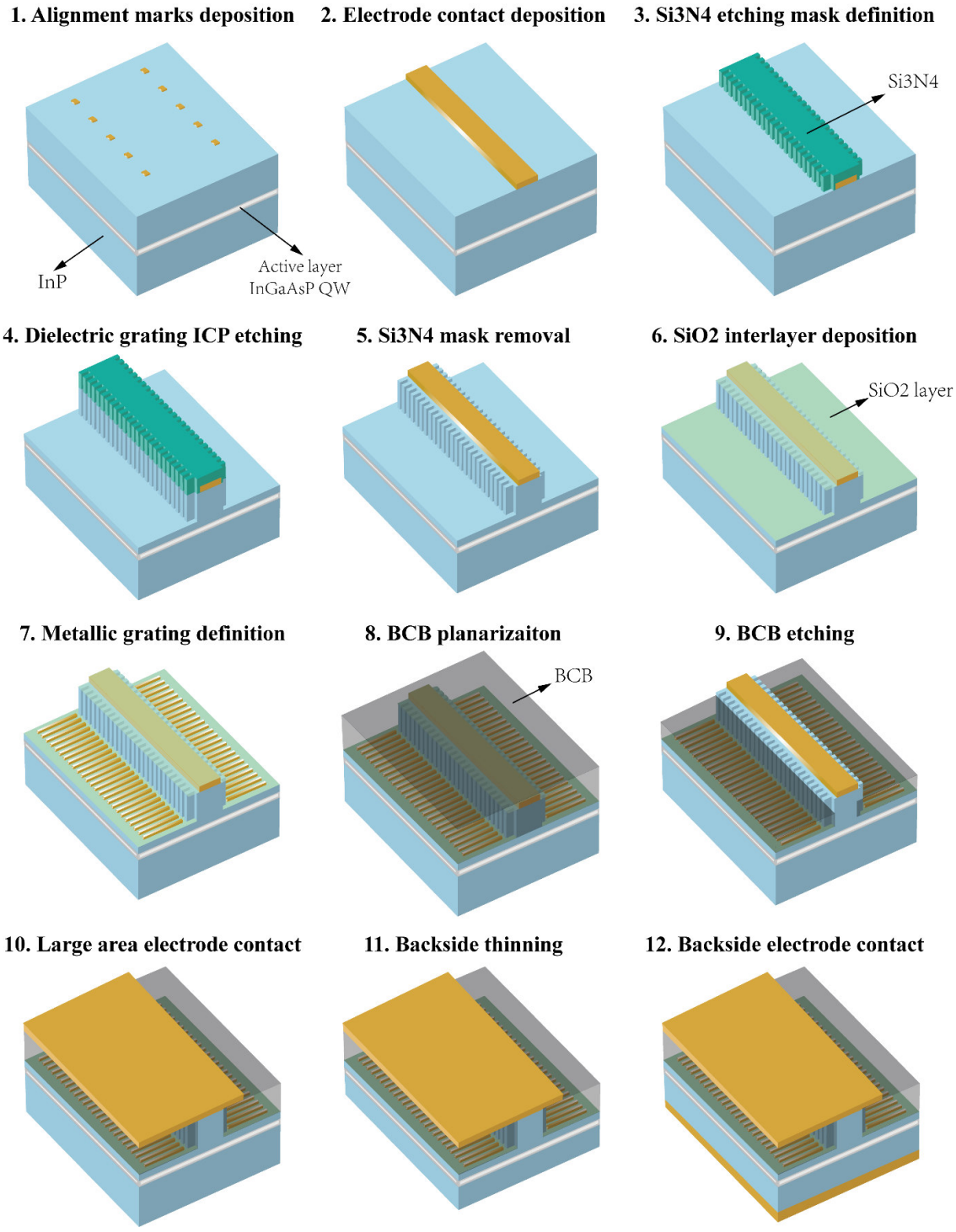

Figure S1. Flow chart of technological fabrication process.

S.2 Experimental characterization setup

The experimental setup used for optoelectric characterizations of DC DFB lasers is shown in **Figure S2**. The electrical voltage supply is obtained using either a TGA1230 waveform generator allowing pulsed operation of different duty cycles, or a Yokogawa 7651 DC source. The electrical current in the circuit is determined by measuring the drop voltage on a 10 Ω resistor using the Tektronix TDS 360 oscilloscope. The emitted optical power is measured using a Melles Griot 13PDC001 optical power-meter equipped with an integrating sphere detector or Agilent 8163A with fiber input. The laser emission spectra are characterized using an ANDO AQ6317B optical analyzer with the finest wavelength resolution of approximately 10 pm.

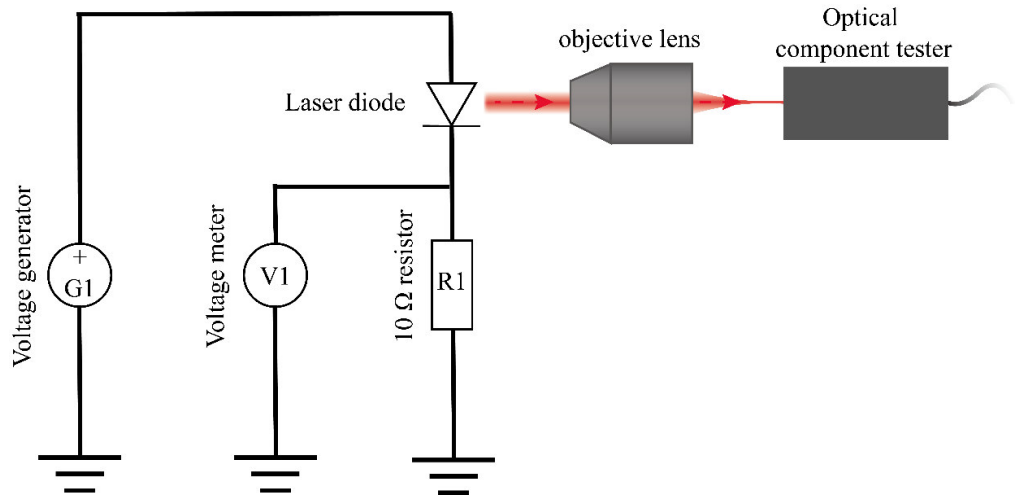

Figure S2. Schematics of the setup used for lasers optoelectric characterizations.

S3. C-C DFB lasers plane-wave model

To perform the modeling of C-C DFB lasers the Abeles transmission matrix method model of a Bragg mirror structure with a complex refractive index profile shown schematically in **Figure S3** is considered.[1] In this model each period Λ is decomposed into 8 layers of thickness Λ/8 (Figure S3a). The spatial phase shift ψ between the rising edge of real and imaginary refractive index modulations is equal to an integer number m of $\pi/8$ (i.e. m×45°). The real part of the index profile over a half-period Λ/2 equal to $N_{Re+}=n_{eff\ WG} + \Delta n_{Re}/2$ and over the next half-period is $N_{Re-}=n_{eff\ WG} - \Delta n_{Re}/2$. In turn the imaginary part over a half-period is equal to $N_{Im-}=-ig + i\Delta n_{Im}$ and over the next half-period is $N_{Im+}=-ig$ where g is the variation of the imaginary part of the related refractive index to the introduction of gain into the structure. For the C-C DFB lasers considered in out study ψ=0, while for metallic grating DFB lasers $\Delta n_{Re}=0$.

The threshold gain level can be determined by modeling the DFB laser array with such 1D periodic stack of layers of thickness Λ/8 whose refractive index matches the effective index of the Bragg waveguide at the corresponding position along the light propagation axis as shown in Figure S3b. The facets termination is taken into account by adding left and right zones with incomplete period. The length of these zones may be arbitrary and is not bounded by the condition to be an integer number of Λ/8. For convenience the ratio L_{facet}/Λ is denoted as Φ_L and Φ_R for the left and right facets, respectively. The external cavity section of variable length

and the 200 nm thick gold mirror with the material parameters given in Palik,[2] are also included in the Bragg mirror layer stack.

The relevant longitudinal mode threshold gain g_{th} can conventionally be determined from the observation condition of the first pole of the transmission matrix of such a 1D periodic structure. According to the experimental results obtained in Parity-Time symmetric DFB lasers, similar to that used in our study, but with 3rd order Bragg grating, the amplitude of the modulation of grating refractive index profile $\Delta n_{Re}=0.002$ and $\Delta n_{Im}=0.0004$.[3] It is namely these values that have been used in our modeling study. To get an idea, an imaginary refractive index $ig = 10^{-4}$ at a wavelength of 1.55 µm corresponds to a gain level G = 35.21 dB/cm.

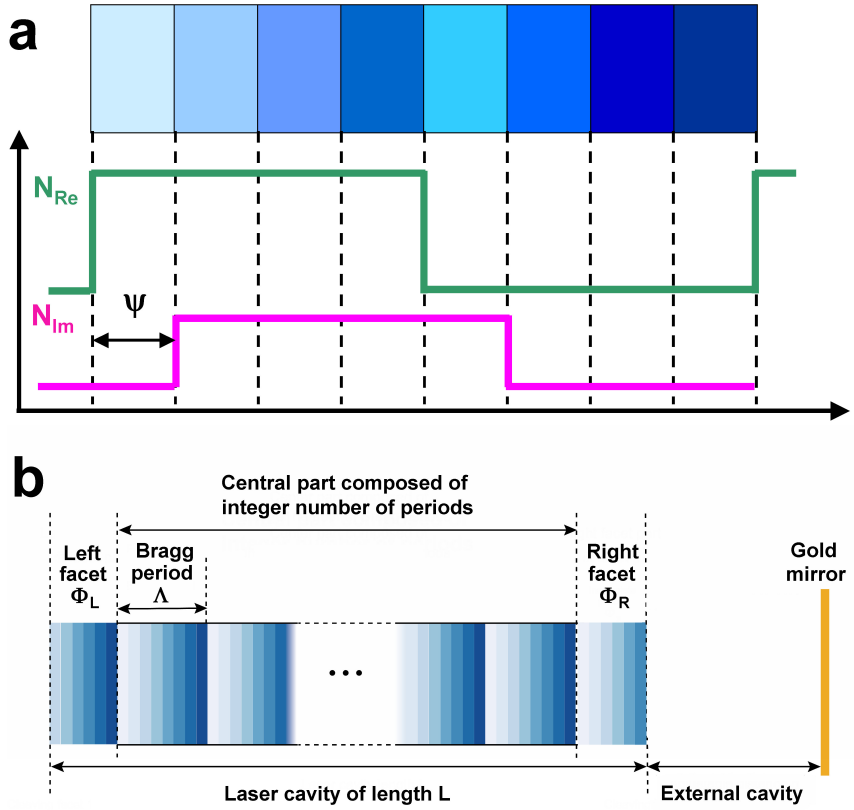

Figure S3. a) Schematic of the complex index profile Bragg grating period modeled by the Abelès transmission matrix method. Each period Λ is composed of eight equal-thickness Λ/8 layers with complex refractive index values $N_{Re}+iN_{Im}$. b) Schematic of the complex index profile Bragg grating with external cavity formed by gold mirror.

References

[1] M. Born and E. Wolf, Principles of optics: electromagnetic theory of propagation, interference and diffraction of light, Elsevier, **2013**.

[2] E. D. Palik, Handbook of optical constants of solids, Academic press, **1998**.

[3] V. Brac de la Perrière, Q. Gaimard, H. Benisty, A. Ramdane, and A. Lupu, *Nanophonics*. **2021**, 10, 1309–1317.